LRP 387/89 October 1989

EXPERIMENTAL RESULTS ON A 100 GHz FREQUENCY TUNABLE QUASI-OPTICAL GYROTRON

S. Alberti, M.Q. Tran, J.P. Hogge, T.M. Tran,
A. Bondeson, P. Muggli, A. Perrenoud, B. Jödicke
and H.G. Mathews

submitted for publication in

Physics of Fluids B

Experimental results on a 100 GHz frequency tunable quasi-optical gyrotron.

S. Alberti, M. Q. Tran, J. P. Hogge, T. M. Tran, A. Bondeson
P. Muggli, A. Perrenoud+, B Jödicke*, and H. G. Mathews*

Centre de Recherches en Physique des Plasmas
Association Euratom-Confédération Suisse
Ecole Polytechnique Fédérale de Lausanne
21, Av. des Bains, CH - 1007 Lausanne, Switzerland

+Present address : Vibro-Meter SA, CH-1701 Fribourg, Switzerland
*Department EKR, ABB-Infocom SA, CH-5401 Baden, Switzerland

Experiments on a 100 GHz Quasi - Optical (Q.O.) gyrotron operating at the fundamental ($\omega = \Omega_{ce}$) are described. Power larger than 90 kW at an efficiency of about 12% was achieved. Depending on the electron beam parameters, the frequency spectrum of the output can be either single-moded or multimoded. One of the main advantage of the Q.O. gyrotron over the conventional gyrotron is its continuous frequency tunability. We have tested various techniques to tune the output frequency, such as changing the mirror separation, the beam voltage or the main magnetic field. Within the limitations of the present setup, 5% tunability was achieved. The Q.O. gyrotron designed for operation at the fundamental frequency, exhibits simultaneous emission at 100 GHz (fundamental) and 200 GHz (2^{nd} harmonic). For a beam current of 4A, 20% of the total RF power is emitted at the second harmonic.

I. INTRODUCTION

For electron cyclotron resonant heating of thermonuclear plasmas, high power CW sources ($P_{RF} \geq 1$ MW) in the 100 - 300 GHz frequency range are needed.[1] The gyrotron has been demonstrated to be the most promising candidate for this application. Two different concepts have been intensively investigated up to now. The conventional gyrotron, where the electronic interaction occurs in a wave guide cavity, has already reached power levels of up to 645 kW at 140 GHz in short pulse operation[2] and 100 kW in CW operation.[3]

The second concept, which is the subject of this paper, is the quasi-optical gyrotron[4,5] and uses an open, quasi-optical Fabry-Perot resonator operating in the millimeter wavelength range. Two important features characterize this device: a continuous frequency tunability (by changing the mirror separation and the DC magnetic field), and secondly, for high power CW operation, a cavity volume, larger than the conventional gyrotron, which allows the operation at higher frequency ($f \geq 200$ GHz), while keeping the power density due to ohmic losses on the resonator wall below the limit of about 3 kW/cm^2 .[6-8] The interaction of the electron beam with the RF field of the resonator occurs with $TEM_{0,0,q}$ Gaussian modes. Due to the large mirrors separation, many longitudinal modes can be excited simultaneously, however, a theoretical study of multimode competition[7] has shown that single-mode excitation can occur at high current. The experimental observations which are presented in this paper (in agreement with other, similar, experiments[9,10]) show that single-mode or nearly single-mode operation is possible for beam currents up to 10 A.

The paper is organized as follows. The experimental test-stand, the electron beam parameters, the small and large resonators, as well as the diagnostics are presented in section II. Section III is devoted to the experimental results and is divided in two subsections; one for a small resonator, and the other one for a large one. The discussion of the results is made in section IV. The main difference between the small and large resonator configuration being that the former operates completely in the soft excitation regime while, for the latter, the main excited mode can be in the hard excitation regime. In addition, for the large resonator, excitation of the 2^{nd} harmonic (200 GHz) has been observed. A brief summary of the results (Section V) will finally conclude the paper.

II. EXPERIMENTAL SETUP

All the experiments were performed in the CRPP large test stand (Fig. 1 a) . A temperature-limited MIG electron gun, operating at voltages up to 70 kV and currents up to 11 A, generates an annular electron beam with a mean radius r_b = 2.13 mm, a velocity pitch $\alpha \equiv < v_\perp/v_\parallel > \cong 1.49$ and a pitch angle dispersion $\Delta\alpha/\alpha$ = 21%. This gun was designed using the Hermannsfeldt code[11]. The relatively high pitch angle dispersion is due to the use of a gun which was optimized for operation at 120 GHz and not at 100 GHz. The numerical simulations of the efficiency, however, indicates that the Q.O. gyrotron is relatively insensitive to spread in α. The magnetic field profile is generated by a system of 4 superconducting coils composed of a pair of Helmholtz coils operating at magnetic field of up to 4 Tesla, and a pair of gun coils at the cathode region. A magnetic field compression of about 20 between the cathode and the interaction region can be achieved with this coil arrangement (Fig.1 b). A large diameter vacuum vessel (diameter $\approx$ 40 cm) is mounted in the inner bore of the Helmholtz coils. It accommodates the beam ducts, interchangeable Fabry-Perot resonators of various sizes, and the collector (see Fig. 1). Table 1 summarizes the beam properties at the interaction region as obtained from a numerical optimization of the magnetic field profile.

Two, different, symmetric resonators have been used in this experiment. They were designed using a computer code[12], based on Kirchoff's formulation of the Huygens-Fresnel principle which gives the resonator quality factor Q for a given $TEM_{0,0,q}$, mode and the coupling efficiency ε_c, which is defined as the ratio of the power collected through the output waveguide to the total diffracted power. Benchmarking of the code

was performed by low-power measurements of the resonant frequency and the resonator Q value[13]: a satisfactory agreement between calculations and experiment was found. For the "small resonator", the mirrors have a 5 cm radius of curvature and a diameter of 1.9 cm. The separation, d, between the mirrors is adjustable from 4 to 6 cm. The "large resonator" has mirrors of 50 cm radius of curvature and 13.6 cm diameter, with separation d of 32.9 - 34.9 cm. Experiments with the large resonator were performed with and without a cylinder (diameter = 15 cm) inclosing the whole resonator. This cylinder is similar to the magnet cross bore of the compact version of a Q.O. gyrotron.[10] We did not observe however any influence on the performances of our device.

The output coupling is purely diffractive for both cavities. For the small resonator, diffraction occurs around the edge of the mirror while for the large one, the RF power is coupled out through annular slots in the output mirror (Fig. 2)[14]. The ohmic losses on the mirrors are on the order of 5% and the output coupling efficiency is 90% for the large resonator. For the small resonator, this factor is more difficult to estimate since we cannot model, nor measure, the fraction of power collected through the output waveguide. Because of the high diffraction losses for the higher-order transverse modes ($TEM_{m,n,q}$ $m \geq 1$, $n \geq 1$), only the fundamental Gaussian mode ($TEM_{0,0,q}$) has a quality factor high enough to allow oscillation to start. The total quality factor (including diffractive and ohmic losses) is 5100 ($TEM_{0,0,27}$), and 33200 ($TEM_{0,0,227}$) for the small and the large resonators, respectively. The computed total Q for the large resonator at the second harmonic ($TEM_{0,0,454}$) is 870000 with a transmission of 0.036%. The separation of the mirrors (3.94 cm and 33.9 cm) results in a longitudinal mode spacing of 3.7 GHz and 0.444 GHz, respectively. The properties of the resonators are summarized in Table II.

Because the resonator is symmetric, an equal amount of RF power flows through two overmoded waveguides (diameter = 8.69 cm) towards two, 125-μm thick, kapton vacuum windows. The kapton windows withstand a power density of up to 1.5 kW/cm^2 during 15 ms without any damage.We are limited to a pulse length of about 15 ms because the mirrors and the collector are not cooled. In order to avoid perturbation of the resonator field in the interaction region, the electron beam is not confined by a beam duct in that region over a distance of approximately 12 cm (i.e. 8 spot sizes).

Several diagnostics have been used to measure the relevant parameters in this experiment. For the RF power level measurement two calorimetric systems were used. A Scientec laser calorimeter was modified by adding a thicker absorptive layer (3M Nextel spray or paint) to maximize the absorption in the 100 GHz range. This calorimeter can withstand a maximum power density of 200 W/cm^2. At high power, the Nextel coating burned and needed to be reapplied periodically. A second calorimeter was built, using Octanol[15] $C_8H_{18}O$ as the absorbing medium.[16] Octanol was selected because of its high boiling point (Boiling point = 195 °C) and its dielectric properties at millimeter wavelengths. No power limitation was observed with this calorimeter at up to 10 - 15 kW/cm^2. The measured reflection was less than 5%.

To determine the spurious second harmonic content, we employed the same technique as Byerly et al.[17], who inserted into the microwave beam an absorber (Macor or Nylon 6.6.) which has different absorption coefficients [18,19] at 100 and 200 GHz. To avoid inaccuracy due to reflections, the absorber plate thickness T is equal to $n2\pi c\sqrt{\varepsilon_r}/\omega$, where ω is the fundamental frequency and n is an integer. Thus, the plate is always matched to both the fundamental and harmonics since ε_r is approximately constant over this

frequency range. Second harmonic emission was also directly monitored via a high-pass band filter with an attenuation of at least -60dB at 100 GHz.

The polarization of the output RF field was measured by reflecting the EM wave on a one dimensional grid (wire diameter = 10μm, wires separation = 100 μm) and collecting the reflected power through a rectangular microwave horn (Fig. 3). In Figure 4 is shown the frequency measurement setup which consists in a two stage heterodyne detection.

The RF signal is down converted to an IF signal at 8-12 GHz via an harmonic mixer operating at the 8th harmonic ($f_{RF} = 8\, f_{LO} + f_{IF}$). The IF signal is amplified (30 dB) and filtered by a narrow band-pass filter (center frequency 8.150 GHz and $\Delta f = \pm 50$ MHz) and is, again, down converted to 200 MHZ. (The band-pass filter avoids the uncertainty due to image generation in the last mixer.) The 200 MHz signal is then fed into a logarithmic amplifier. By a fast sweep of the local oscillator frequency (f_{LO}), it is possible to obtain a spectrum of the gyrotron output over a 3 GHz bandwidth, in 500 μs. In addition the measurement of the relative power level between longitudinal modes, when multimode emission occurs, has to be taken with some care. This is due to the fact that we operate the harmonic mixer at a fairly high harmonic (8^+); therefore, the conversion loss is strongly dependent on the RF frequency (even within the separation of two longitudinal modes) and the LO power. According to the manufacturer[20], the most reliable measurement at high harmonic number is obtained by maximizing the LO power in order to saturate the diode. All the measurements were performed according to this criterion.

III EXPERIMENTAL RESULTS

The measurements presented in this section were performed on the two resonator configurations (small and large).

A) Small resonator

A typical experimental trace, showing the temporal evolution of the applied beam voltage V_b, the intermediate anode voltage V_a, the beam current I_b, and the 100 GHz signal are shown in Figure 5. A minimum starting current of 800 mA was observed for the $TEM_{0,0,27}$ mode. Optimization of the power output was achieved by varying the static magnetic field in the gun region and the magnetic field in the resonator region. Due to the relatively large separation between longitudinal modes ($\Delta f/f = 3.7\%$) with respect to the instability bandwidth ($\approx 5\%$), the gyrotron frequency remained constant during this procedure. We also checked that the electron beam was properly centered with respect to the resonator axis by shifting the latter in the direction perpendicular to the static B field.

The results of this optimization process are summarized in Figure 6, where we present the maximum output power versus detuning $\Delta\omega / \omega$ ($\Delta\omega / \omega = 1.- \Omega_{ce}/\gamma_0\omega$) for beam currents ranging from 3 - 10 A at a fixed beam energy of 70 kV. A maximum output power of 48 kW at 10 A of beam current was observed in single-mode operation, corresponding to a total efficiency of $\approx 7\%$.

The measured emitted power in the polarization corresponding to an electric field, $\underline{E}_\perp$, perpendicular to the static magnetic field $\underline{B}_0$ was 6 dB

higher than the power in the polarization corresponding to, $\underline{E}_{//}$, parallel to $\underline{B}_0$ (see Fig.3).

B) Large resonator

Compared to the previous resonator, the large resonator has a higher spectral density (444 MHz between longitudinal modes), and the total quality factor is increased to 33200. As with the small resonator, we carried out an extensive optimization on the beam parameters was performed in order to maximize the output power. In this process, we verified, at first, that the annular electron beam is correctly centered with respect to the resonator. The relation between the "pencil-beam efficiency" η_{pb} and the "annular-beam efficiency" η_a is given in the linear theory by :

$$\eta_a = \eta_{pb} \frac{1}{2} [1 \pm \cos(2ka) J_0(2kr_b)]$$

where a is the distance between the beam center and a node (+) or a maximum (-) of the RF field, k is the wave number, and J_0 is the ordinary Bessel function of zeroth order. The experimental results (Fig. 7), which are obtained by moving continuously the whole resonator with respect to the beam, are in agreement with the theoretical prediction. We then fixed the magnetic field in the interaction region and optimized the output power by changing the currents in the two gun coils. At the optimum, the pitch angle α is 1.12 and the beam radius is 2.23mm; calculated from the Hermannsfeldt code using the optimized B_0 field value. We shall use these values for the analysis of all the results.

A minimum starting current of 100 mA was observed at 100.169 GHz ($TEM_{0,0,225}$). As the beam current is continuously increased from the mini-

mum starting current to 10A, we observed that even for the single-mode operation the excited longitudinal mode is current dependant, varying from $TEM_{0,0,225}$ at I_b = 0.1A to $TEM_{0,0,229}$ at I_b = 10A (Fig. 8). Typically 4 to 5 modes are excited between these current limits. A typical experimental spectrum, showing single-mode oscillation at a beam current of I_b = 9.4 A, is shown in Figure 9a. At a beam current of I_b = 10A, a nearly single-mode spectrum is observed (Fig. 9b). In the same beam current range (i.e. I_b = 11 A), a multi-mode spectrum is shown in Figure 9c.

Figure 10 shows the frequency tunability by changing the mirror separation at I_b = 3A. The squares indicate the main excited mode. In the case of multimoding (maximum 3 modes), the neighboring modes are typically 10 dB lower than the main mode. A variation of the DC magnetic field in the interaction region from -3% to +2% around the optimized value for the 100 GHz operation, permits a corresponding frequency tunability without observing a degradation in the output power (Fig.11). Variation of the DC magnetic field beyond these limits is not possible because of technological constraints on the electron gun (beam interception on the intermediate anode for too low magnetic fields), and on the superconducting magnet system itself (danger of quenching at higher magnetic fields). Because the relativistic cyclotron frequency is energy dependent, a frequency tuning of the radiation is also possible by varying the beam acceleration voltage (Fig. 12). The drop of the output power for voltages higher than 71 kV is probably due to a degradation of the beam properties.

The power content of the radiation at the fundamental and second harmonic frequencies was measured at a beam current of 4A (Fig.13). The scatter of the points on this graph limits the accuracy of the fit of the experimental data with the theoretical curves. However, we can say that 25%±10% of the total power is emitted at the second harmonic. A verification of this mea-

surement was performed by measuring the total power after the Macor absorber with a diode detector instead of the Scientec calorimeter. The two results were in good agreement.

The total power versus beam current (i.e without discriminating between fundamental and second harmonic) is shown in Fig.14. Taking into account the reflectivity of the Scientec and the octanol calorimeter, both diagnostics give the same results within the experimental uncertainty. A maximum RF power of 90 kW has been obtained for pulse lengths up to 10 ms. This power measurement corresponds to a total efficiency of 12%. As in the small resonator, the polarization measurement yields about 6dB difference between the cross polarizations, the dominant polarization being the same as for the small resonator.

IV DISCUSSION

A general observation concerning the electron beam properties, which is valid for the interpretation of the results obtained on both cavities, is that the experimental optimization of the RF power against the pitch angle α leads to an optimized $\alpha_{opt} = 1.12$; which is lower than the design value of $\alpha = 1.45$. Note that in the interaction region the electron beam depression is not taken into account in the beam simulation.

Let us first discuss the results obtained with the small resonator. Taking into account the above remark (i.e. $\alpha_{opt} = 1.12$) the experimental minimum starting current, $I_{stmin} = 0.8$ A, is close to the theoretical value of 0.9 A for $\alpha = 1.12$. The experimental measurement of the instability bandwidth (Fig. 6), and the fact that no multimode emission was observed, indicate that the single-mode theory is consistent with the experiment. For beam currents up to 10 A, we could obtain single-mode operation, with a maximum output power of 48 kW; which yields to a total efficiency of $\eta_{tot} = 7\%$.The corresponding electronic efficiency η_{el}, taking into account the ohmic losses and the output coupling efficiency, is then given by

$$\eta_{el} = \frac{\eta_{tot}}{\varepsilon_c} (1 + \varepsilon_\Omega)$$

where ε_c is the coupling efficiency and ε_Ω is the ratio between ohmic and diffractive losses. For the small resonator, ε_Ω is about 0.065. Assuming a coupling efficiency $\varepsilon_c = 0.9$ we obtain a maximum electronic efficiency of $\eta_{el} \cong 8.5\%$. The discrepancy with the theoretical prediction, which gives $\eta_{el.th} = 11\%$, might be due to the uncertainty in the beam properties in the interaction region.

In terms of the normalized parameters F,μ, Δ[21,22] for the small resonator the normalized interaction length μ is about 4 - 5. When reported in the [I, μ] diagram[22], this value corresponds to an operation in the soft excitation regime. For the large resonator, due to the larger beam waist, the interaction length μ is about 12 - 15. Thus the high efficiency region is completely in the hard excitation region and is, therefore, not accessible in single-mode operation. In this case, the high efficiency region is only accessible when the external electron-beam (α,γ,I_b) parameters are ramped or when multimode competition occurs.

Experimentally, for the large resonator, we observed that single-mode operation (Power of spurious modes < -12 dB of Power in main mode) or nearly single-mode operation (Power of spurious modes < -5 dB of Power in main mode) is possible at high current up to 11 A (Fig. 9a and 9b). Nevertheless, under different beam conditions (i.e. small variation of α and γ), we could obtain, for the same total efficiency and the same beam current, either single-mode or multimode operation. Following the remark made in Section II, the measurement of the power distribution among the different modes could bear some uncertainty. In any case, from the spectra (Fig.9b) we observed that only one mode was preferentially excited. The study of frequency tunability by changing the mirror separation d (Fig. 10), has shown that the main excited mode always has the same parity; meaning that one excites preferentially either the TEM $_{0,0,2q}$ or TEM $_{0,0,(2q)-1}$ modes, depending on the relative position of the center of the annular electron beam and the resonator center. The frequency tunability associated with a variation of the DC magnetic field (Fig. 11) is approximately 5% around the normal operating frequency. As it has been discussed previously, the frequency pushing that occurs when the beam current is varied from the minimum starting current

(100 mA) to the maximum (10A), corresponds to a sequence of 4 - 5 modes. A comparison between the experiment and the linear single-mode theory is made in Figure 15. The experimental frequency versus beam current data (Fig 8.) is compared, firstly, with the linear single-mode bandwidth versus beam current curve, and secondly, with the same curve, but taking into account the change in γ due to space-charge. The theoretical linear single-mode bandwidth curves, reported on Figure 15, correspond to the high frequency part of the spectrum which is accessible above the minimum starting current. The space-charge leads to a beam voltage depression in the interaction region given by formula (9) of Ref.10. From this comparison it is clear that, for some beam currents, the excited modes are outside the linear excitation region, and therefore, in the hard excitation region. Two experimental observations give a possible explanation of this fact. First,it should be noted that a stationary state of the intermediate anode voltage V_a, and the beam current I_b (Fig.5), is reached on a time scale on the order of several ms, this time scale is at least two orders of magnitude larger than the resonator filling time ($t_c \approx 0.1$ μs), and the multimode evolution time scale[23] ($t_m \approx 2$ μs): a natural ramping of the external parameters does occur. Second, even in nearly single-mode operation, a multimode competition occurs, either with the fundamental neighboring modes, or with the second harmonic. On figure 15, one can see that the total RF-power versus beam current exhibits jumps at currents corresponding to mode mode switching (I_b = 1.8 A, 2.5 A) or when a multimode regime is excited (I_b = 4.5 A). A maximum output power of 90 kW is reached at 11A, which corresponds to a total efficiency (at the fundamental and the second harmonic) of η_{tot} = 12%. Taking, again, into account the coupling efficiency and the ohmic losses, the corresponding total electronic efficiency is estimated to be about 14%. A direct comparison with the theoretical electronic efficiency $\eta_{el.th}$ = 22 %, which was computed ignoring the second harmonic, is ,however, not possible since

second harmonic emission was detected for currents higher than 0.6 A. The total experimental efficiency of 12% is the efficiency resulting from the emission at the fundamental and second harmonic (No higher harmonics were observed). For a beam current of 4A, the ratio of power between the second and first harmonic is ≈ 20%.We have evidence that, depending on the beam current a strong competition between the fundamental and second harmonic occurs.

V. CONCLUSION

The operation of the 100 GHz Q.O. gyrotron in two different resonator configurations has been demonstrated. The small resonator ($TEM_{0,0,27}$) operated in the soft excitation regime. Powers up to 48 kW at an efficiency of around 7% have been observed in the single-mode operation. Powers up to 90 kW at an efficiency of 12% have been measured in the large resonator at a beam current of 11 A. In the highly overmoded large resonator ($TEM_{0,0,227}$) the oscillation is either single mode or multimode, depending on the beam parameters. For beam currents higher than 2A the oscillating mode is in the hard excitation region. Second harmonic emission was observed for $I_b \geq$ 0.6 A with 20 % of the total power emitted at 200 GHz at a beam current of 4A. These preliminary results have indicated the existence of a strong competition between the fundamental and the 2nd harmonic.

Acknowledgements

This work was partially supported by the Commission pour l'Encouragement à la Recherche Scientifique under grants 1224 and 1564 (1224), by the R and D fund from the Department EKR of ABB-Infocom SA and by the Fond National Suisse de la Recherche Scientifique under grant 2000-005652. We acknowledge fruitful discussion with Drs. A. Fliflet, T. Hargreaves and W. Manheimer from Naval Research Laboratory, and M. Read from Physical Science Incorporated. We would like to thank Dr. T. Goodman for a critical reading of the manuscript.

TABLE 1

Beam properties in the interaction region

Acceleration voltage	$V_b = 70$ kV
Intermediate anode voltage	$V_a = 30$ kV
Beam current	$I_b = 10$ A

	Mean value	Deviation
Beam radius	$< r_b > = 2.13$ mm	$\Delta r_b = 7.6\%$
Pitch angle	$< \alpha > = 1.49$	$\Delta \alpha = 21.\%$
Perpendicular velocity	$< \beta_\perp > = 0.386$	$\Delta \beta_\perp = 5.8\%$
Parallel velocity	$< \beta_{//} > = 0.266$	$\Delta \beta_{//} = 13.1\%$
Relativistic factor γ_0	$< \gamma_0 > = 1.1338$	$\Delta \gamma_0 = 0.023\%$

TABLE 2

Cold resonator characteristics

	Small resonator	Large resonator
Mirror separation d	4.1 cm (4-6 cm)	34 cm (33-35 cm)
Mirror curvature R	5 cm	50. cm
g parameter (g = 1- d/R)	0.18	0.320
Mirror outer diameter	1.9 cm	13.6 cm
Resonator power transmission	3%	4%
Output coupling efficiency ε_c	-	90%
Diffraction Q	5420	34900
Ohmic/diffractive losses	6.5%	5%
Total Q	5100	33200
Beam waist kr_0	10.15	31.7
Longitudinal index q (TEM_{00q})	27	227
c/2d	3.7 GHz	0.444 GHz

References

1 A. C. Riviere, Int. J. Electron. **61**, 693 (1986).

2 K. E. Kreischer, R. J. Temkin, Phys. Rev. Lett., **59**, 547 (1987).

3 K. Felch, R. Bier, L. J. Crag, H. Huey, L. Yves, H. Jory, N. Lopez, and S. Spang, Int. J. Electron, **61**, 701 (1986).

4 G. N. Rapoport, A. K. Nemak, and V. A. Zhurakhovsky, Radiotekh. electron., **12**, 633 (1967).

5 P. Sprangle, J. L. Vomvoridis, and W. H. Manheimer, Phys. Rev. A, **23**, 3127 (1981).

6 T. M. Tran, M. Q. Tran, S. Alberti, J. P. Hogge, B. Isaak, P. Muggli, and A. Perrenoud, IEEE Trans. on Electron. Devices II , **36** , 1983 (1989).

7 A. Bondeson, W. M. Manheimer, and E. Ott, *in Infrared and Millimeter Waves, K. J. Button, editor,* **9**, 309 (1983).

8 A. G. Luchinin and G. S. Nusinovich, Int. J. Electron., **57**, 827 (1984).

9 M. E. Read, M. Q. Tran, J. Mc Adoo, and M. Barsanti, Int. J. Electron., **65**, 309, (1988).

10 A. W. Fliflet, T. A. Hargreaves, W. M. Manheimer, R. P. Fischer, and M. L. Barsanti, Phys. Rev. Lett., **62**, 2664, (1989). A. W. Fliflet, T. A. Hargreaves, W. M. Manheimer, R. P. Fischer M. L. Barsanti, B. Levush and T. Antonsen NRL Memorandum report 6459, Naval Research Laboratory, Washington DC 20375-5000, June 1989.

11 W.B Hermannsfeldt SLAC - Report - 226 , Standford Linear Accelerator Center, Standford, California (1979).

12 A.Perrenoud, T.M. Tran, M.Q. Tran, C. Rieder, and M. Schleipen,Int. J. Electron. **57**, 985 (1984).

[13] A.Perrenoud, M.Q. Tran, B. Isaak, S. Alberti, and P. Muggli in *Proceedings of the 11th international conference of infrared and millimeter waves* , Pisa (Tirrenia 1986), pp. 124-126.

[14] T.A. Hargreaves, K.J. Kim, J.H. McAdoo, S.Y. Park, R.D. Seeley, and M.E. Read, Int. J. Electron. **57**, 977 (1984).

[15] M. N. Afsar, J. Chamberlain, and G. W. Chantry IEEE Trans. Instrumentation and Measurements **IM-25**, 290 (1976)

[16] H. Stickel, Int. J. Electron. **64**, 63 (1988).

[17] J.L. Byerly, B.G. Danly, K.E. Kreischer, R.J. Temkin, W.J. Mulligan, and P. Woskoboinikow, Int. J. Electron. **57**, 1033 (1984).

[18] M.N. Afsar, IEEE Trans. Instrumentation and Measurement, **IM-36**, 530, (1987)

[19] M. N. Afsar and K. J. Button Int. J. IR and MM Waves **3**, 319 (1982)

[20] D. R. Vizard, Farran Technology Ltd., Ballincollig, Cork (Ireland), Private comunication.

[21] G.S. Nusinovich and R.E. Erm, Electron. Tekh., Ser. 1, Elekton. SVCh, 55 (1972).

[22] B.G. Danly and R.J. Temkin, Phys. Fluids **29**, 561 (1986).

[23] M.Q. Tran, A Bondeson, A. Perrenoud, S. Alberti, B. Isaak, and P. Muggli, Int. J. Electron. **61**, 1029 (1986).

Figure captions

Fig. 1 a) Schematic of the quasi optical gyrotron.

1. Helmholtz coils (superconducting)
2. gun coils (superconducting)
3. MIG electron gun
4. SF_6- High Voltage insulation
5. vacuum valve
6. Fabry-Perot resonator
7. waveguide
8. RF windows
9. view ports
10. collector
11. collector coils
12. vacuum pumps

b) DC magnetic field profile

Fig. 2 Output coupling schemes : (a) small resonator. (b) large resonator.

Fig. 3 Setup for the polarization measurement of the RF field at the output window.
a) reflection of the component of the electric field perpendicular to the static magnetic field $\underline{B_0}$ ($\underline{E_\perp}$).
b) reflection of the component of the electric field parallel to the static magnetic field $\underline{B_0}$ ($\underline{E_{//}}$).

Fig. 4 Frequency measurement setup for the 100 GHz signal (fundamental) and the 200 GHz signal (2^{nd} harmonic).

Fig.5 A typical experimental trace , showing the temporal evolution of the applied beam voltage V_b,the intermediate anode voltage V_a, the beam current I_b, and the 100 GHz signal.

Fig.6 Maximum output power versus detuning for the small resonator. The beam energy and the intermediate anode voltage are respectively fixed at 70 kV and 30 kV ($\alpha = 1.12$). The beam current is varied from 3 to 10 A.

Fig. 7 Output power versus relative position a of the electron beam center with respect to the RF field.

Fig. 8 Mode excitation versus beam current (V_b = 70 kV, V_a= 30 kV) for the large resonator.

Fig. 9 Typical frequency spectrum corresponding to 3 different operating regimes:

a) single-mode operation (I_b = 9.4 A, V_b = 70 kV, V_a= 29.5 kV)

b) nearly single-mode operation (I_b = 10 A, V_b = 70 kV, V_a= 30 kV

c) multimode operation (I_b = 11 A, V_b = 70 kV, V_a= 30 kV)

Fig. 10 Frequency tunability by changing the mirror separation d (I_b = 3 A, V_b = 70 kV, V_a= 30 kV, B_0 = 3.96 T). $\Delta d = 0$ corresponds to a mirror separation of 33.8 cm.

Fig. 11 Frequency tunability by changing the DC magnetic field. (I_b = 5.5 A, V_b = 70 kV,V_a= 30 kV, ΔB = 0% corresponds to 3.96 T)

Fig. 12 Frequency tunability by changing the acceleration voltage V_b. (I_b = 2 A, B_0 = 3.96 T,V_a= 30 kV)

Fig. 13 Power content of the radiation at the fundamental and second harmonic (I_b = 4 A, V_b = 70 kV, V_a= 30 kV). A1 and A2 are the proportion to the total power of each harmonic. (A1 + A2 = 1). The continuous lines have been computed using an absorption coefficient of μ_i = 0.75 Np/cm at 100 GHz and μ_i = 2 Np/cm at 200 GHz.

Fig. 14 Maximum total emitted power and efficiency (100 GHz + 200 GHz) versus beam current.

Fig.15 Mode excitation versus beam current (V_b = 70 kV, V_a= 30 kV) for the large resonator. The lower shaded area corresponds to the linear bandwidth versus beam current, calculated for a beam mean radius of $< r_b >$ = 2.23 mm and a mean pitch angle $< \alpha >$ = 1.12, the space-charge voltage depression in the interaction region is not taken into account. The upper shaded area is similar to the previous one, but the space-charge voltage depression in the interaction region is considered. The thick line shows the emitted total power (100 GHz + 200 GHz) versus beam current.

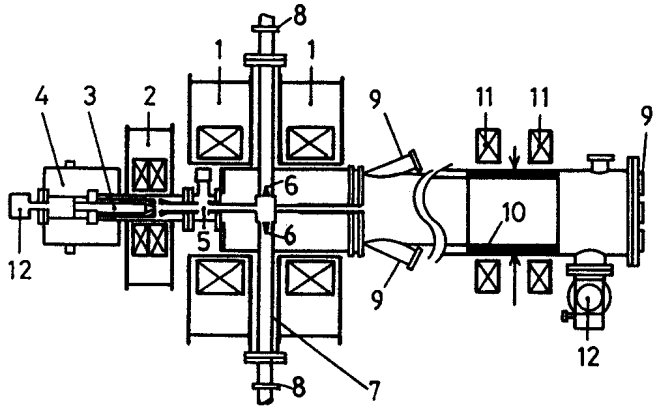

FIG. 1A

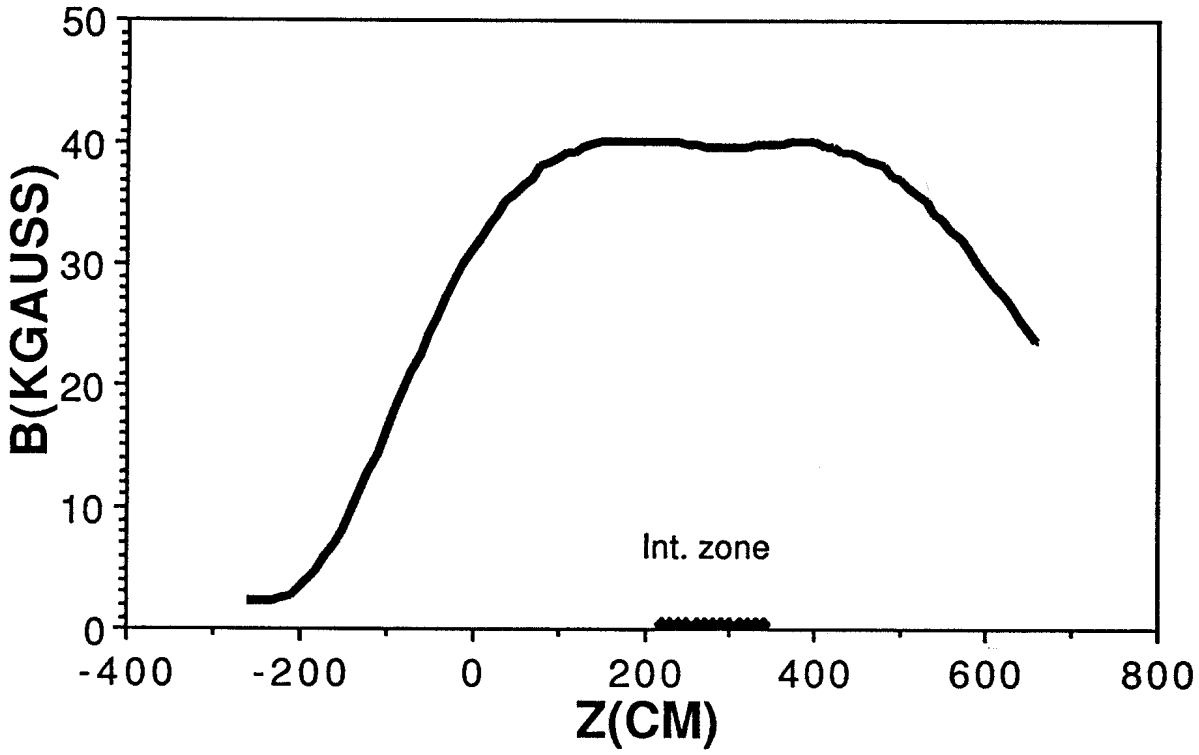

FIG. 1B

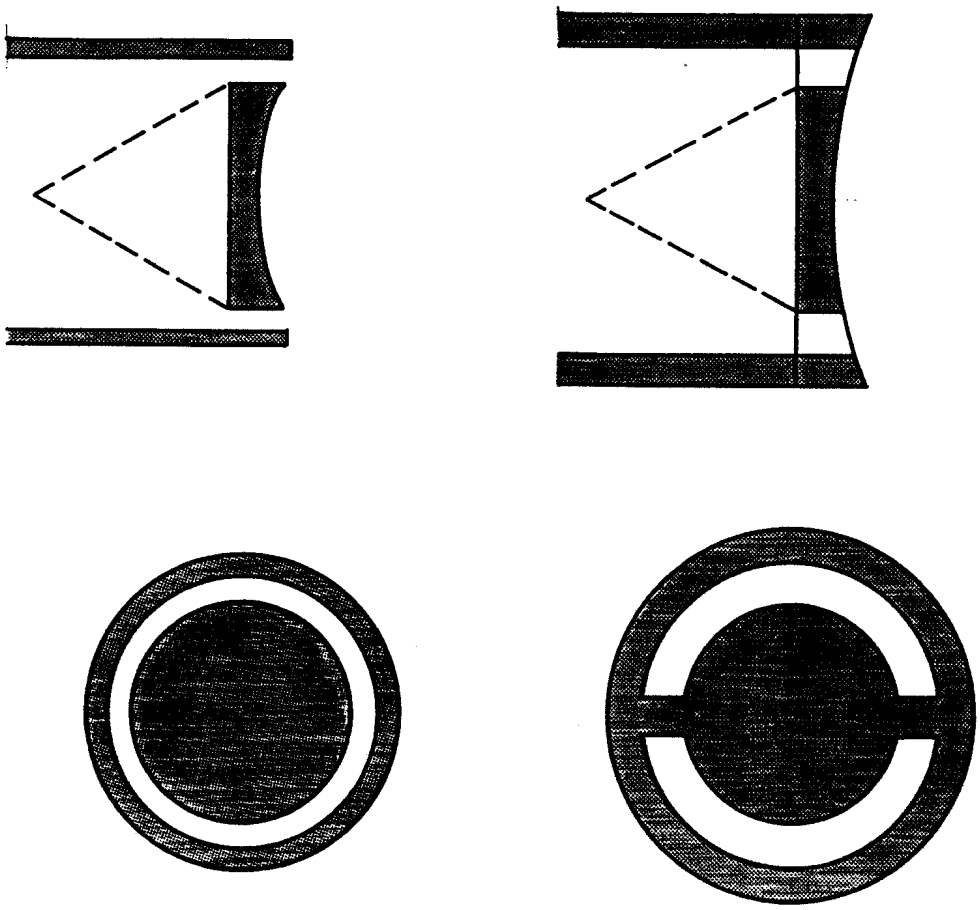

FIG. 2

RF polarisation diagnostic

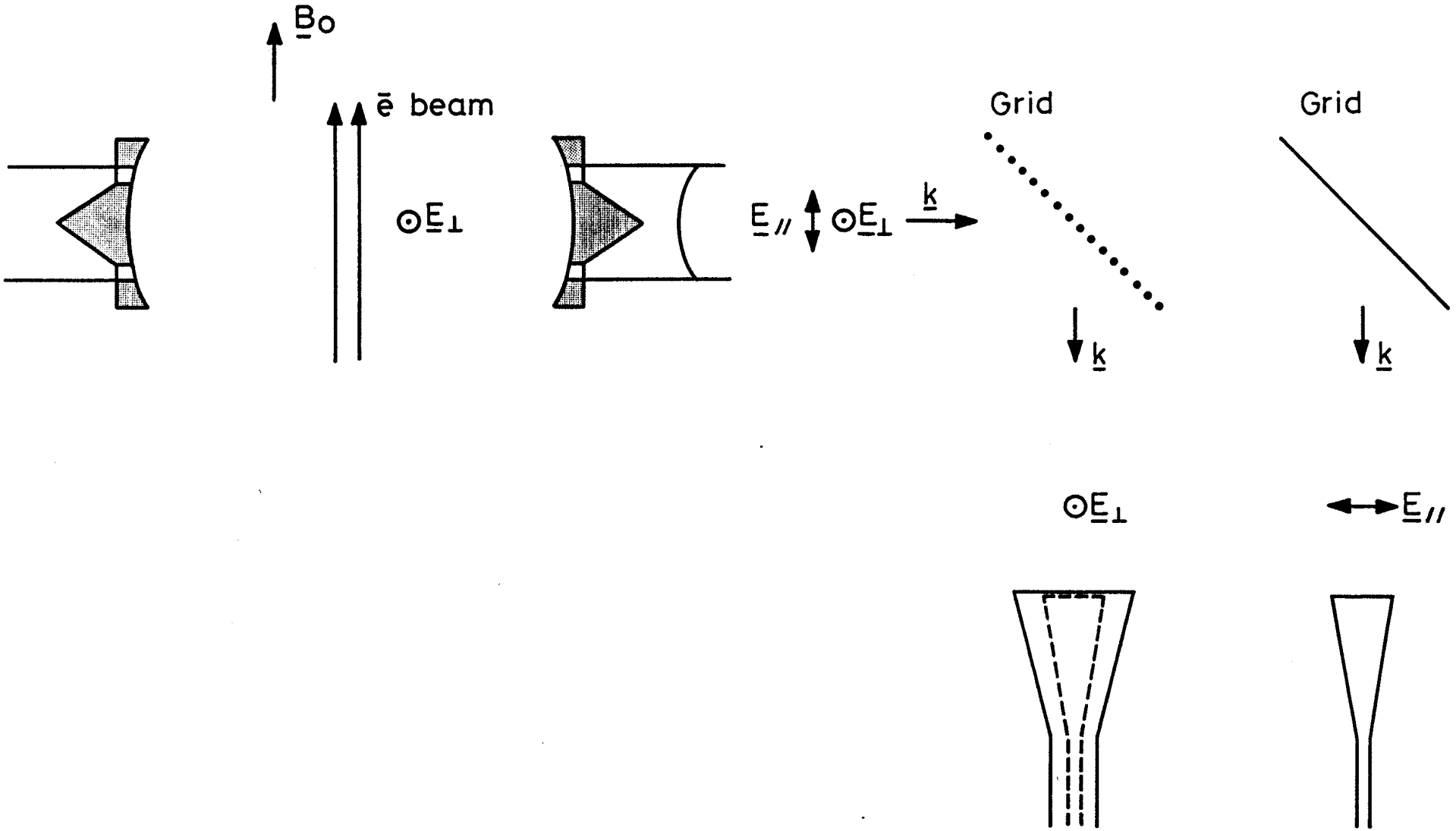

FIG. 3

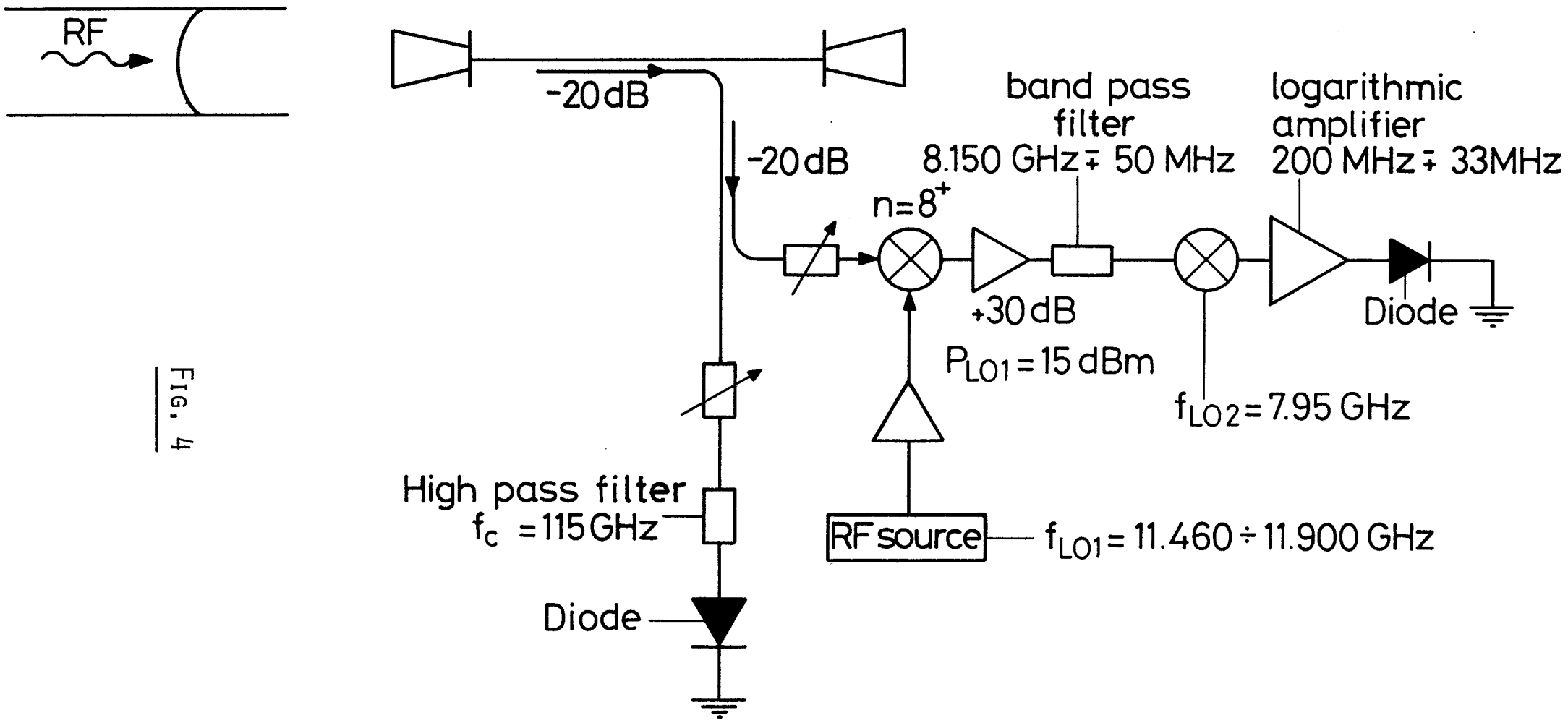
RF
-20dB
-20dB
band pass
filter
8.150 GHz ∓ 50 MHz
logarithmic
amplifier
200 MHz ∓ 33MHz
n=8+
+30dB
Diode
P_LO1 = 15 dBm
f_LO2 = 7.95 GHz
High pass filter
f_c = 115GHz
RF source
f_LO1 = 11.460 ÷ 11.900 GHz
Diode

FIG. 4

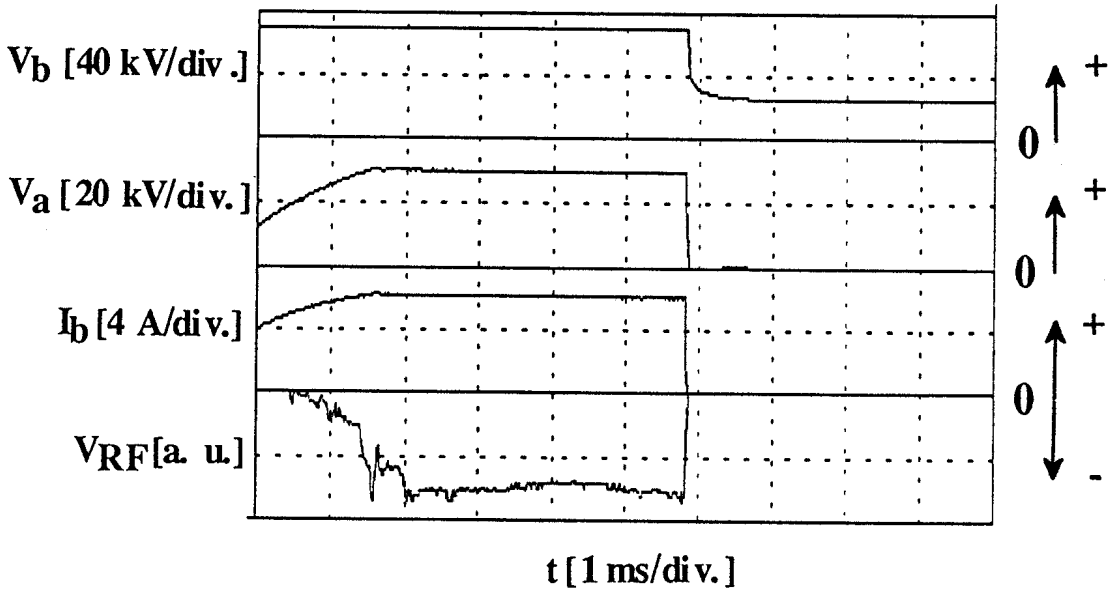

FIG. 5

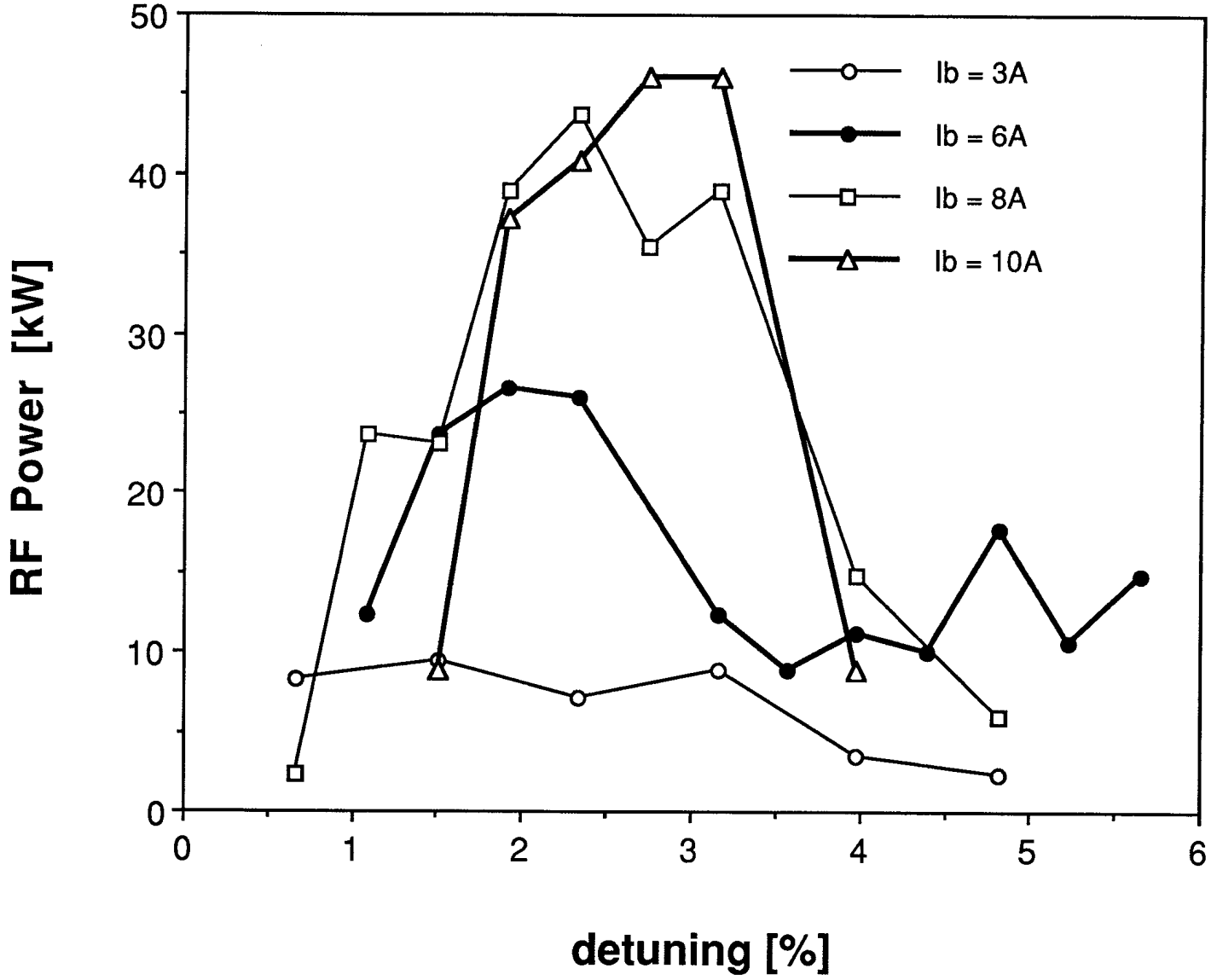
RF Power [kW]
50
40
30
20
10
0
0
1
2
3
4
5
6
detuning [%]
Ib = 3A
Ib = 6A
Ib = 8A
Ib = 10A

FIG. 6

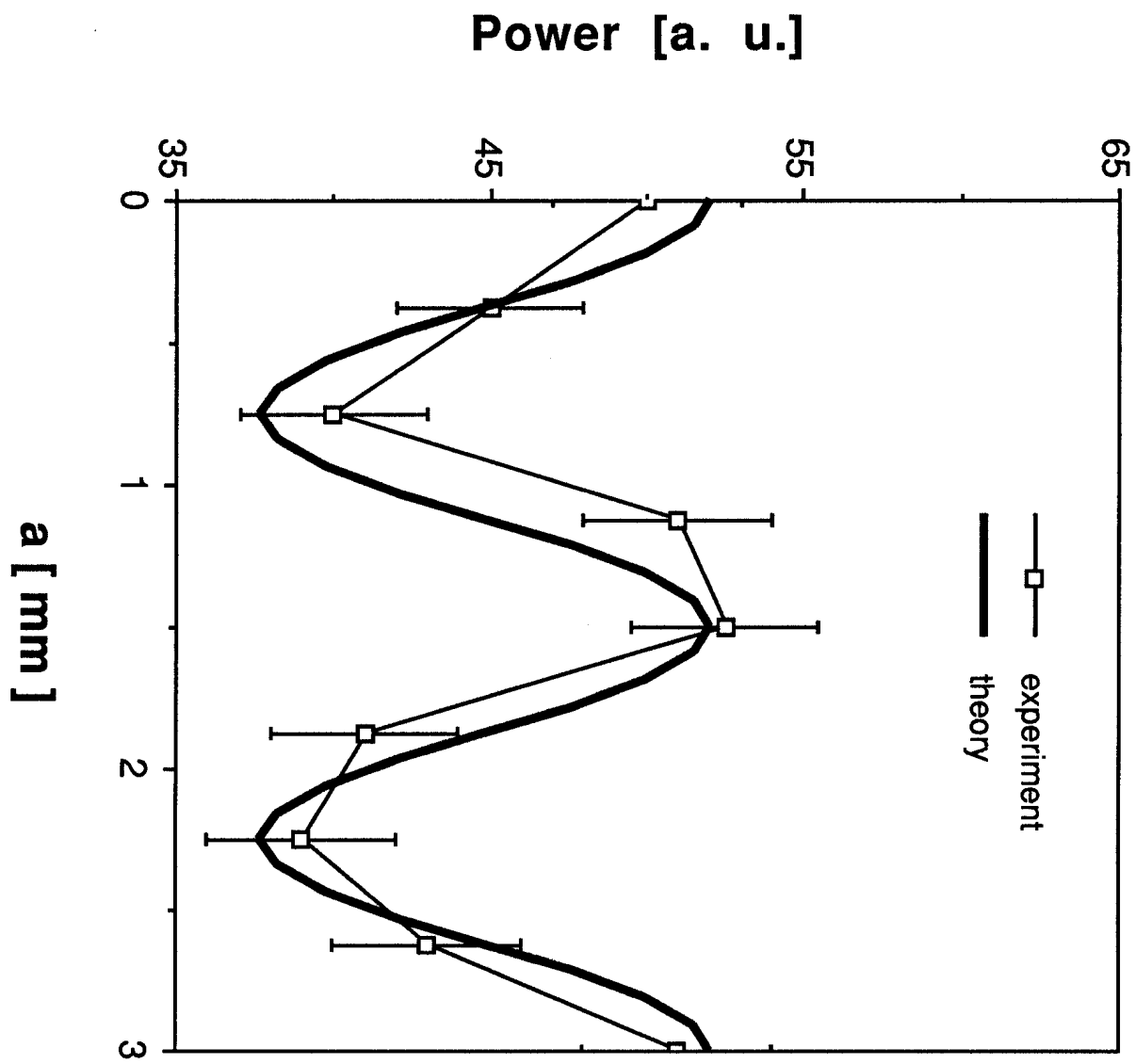

FIG. 7

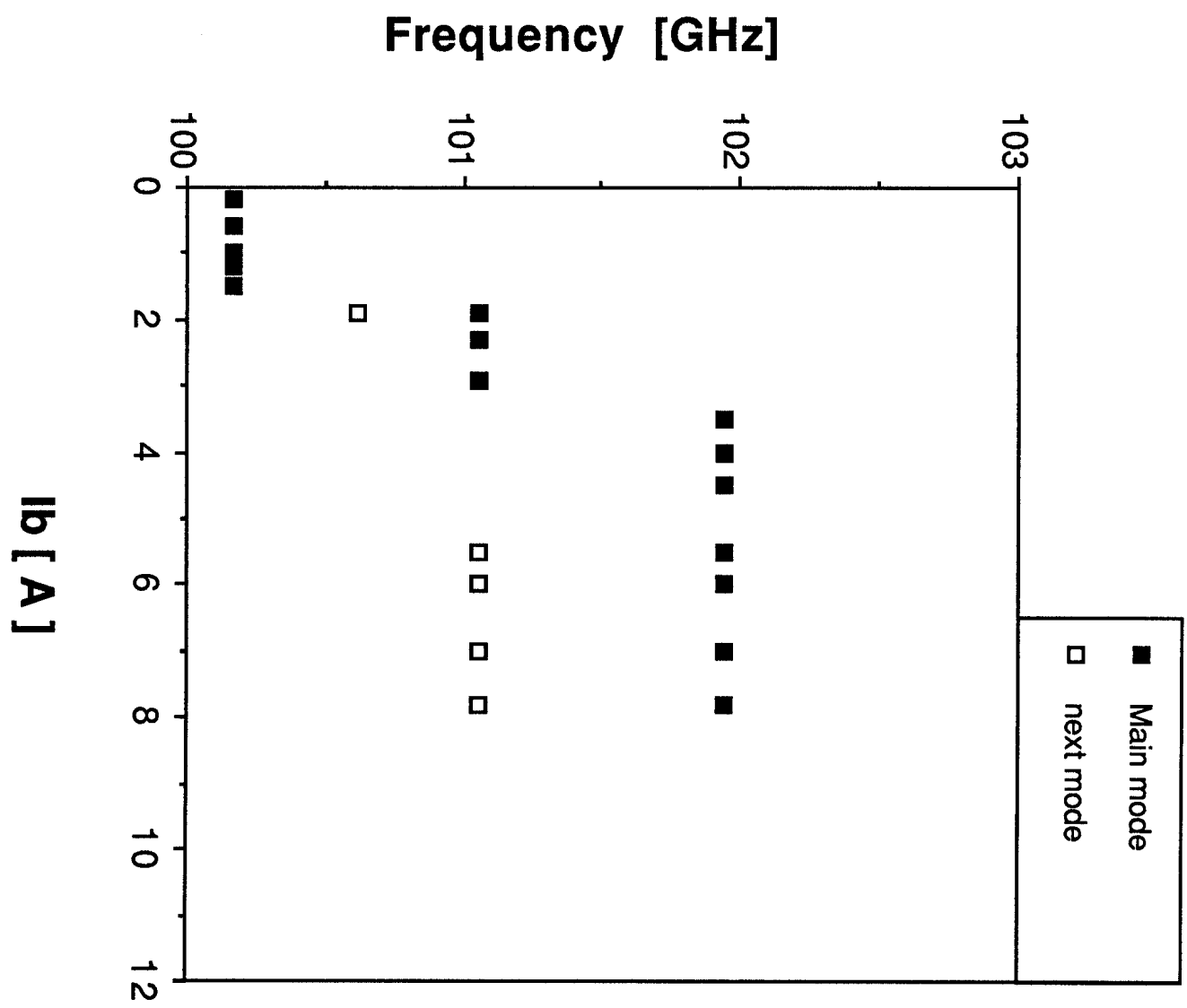
Frequency [GHz]
100
101
102
103
0
2
4
6
8
10
12
Ib [A]
Main mode
next mode

FIG. 8

FIG. 9

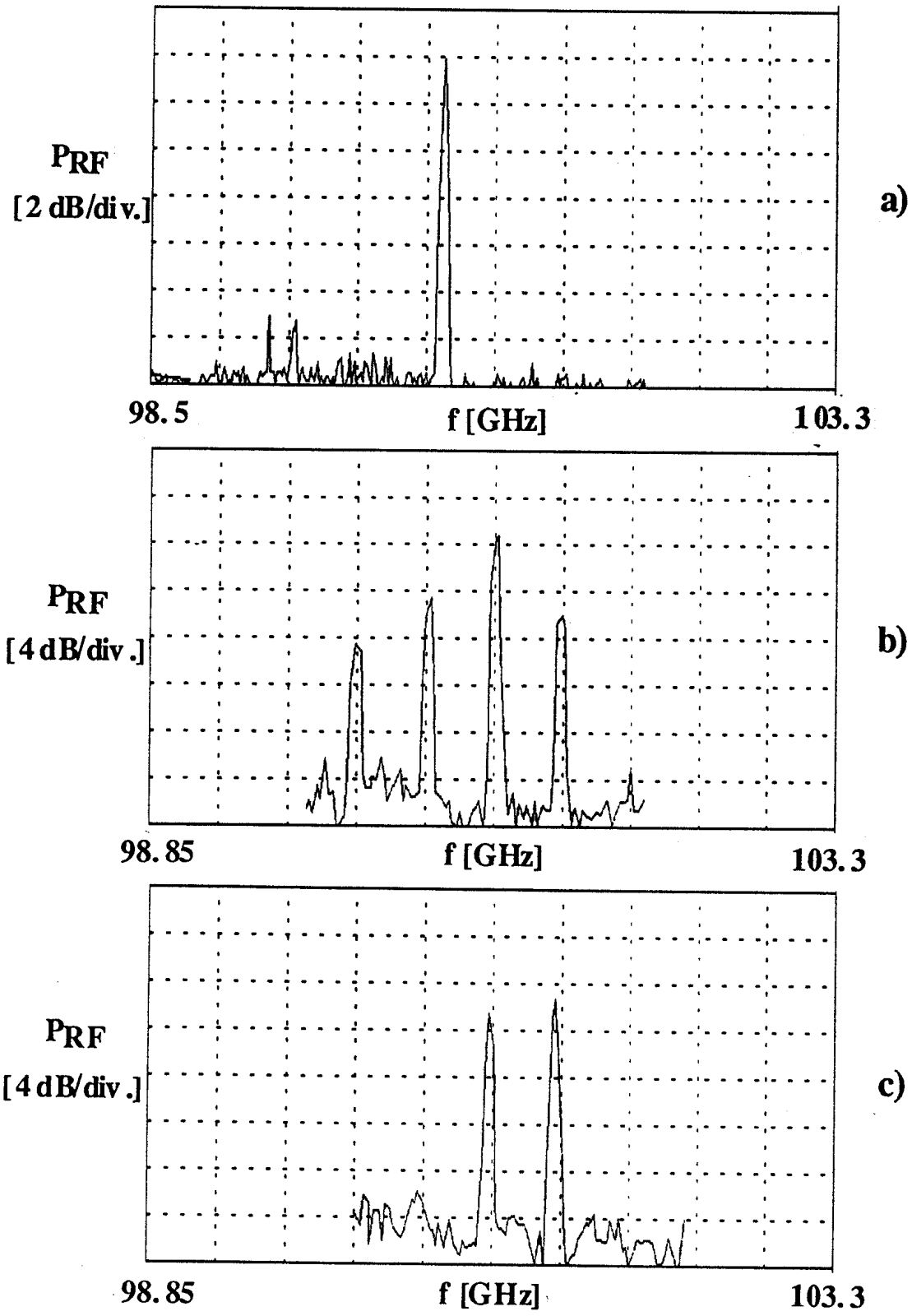
PRF
[2 dB/div.]
a)
98.5
f [GHz]
103.3
PRF
[4 dB/div.]
b)
98.85
f [GHz]
103.3
PRF
[4 dB/div.]
c)
98.85
f [GHz]
103.3

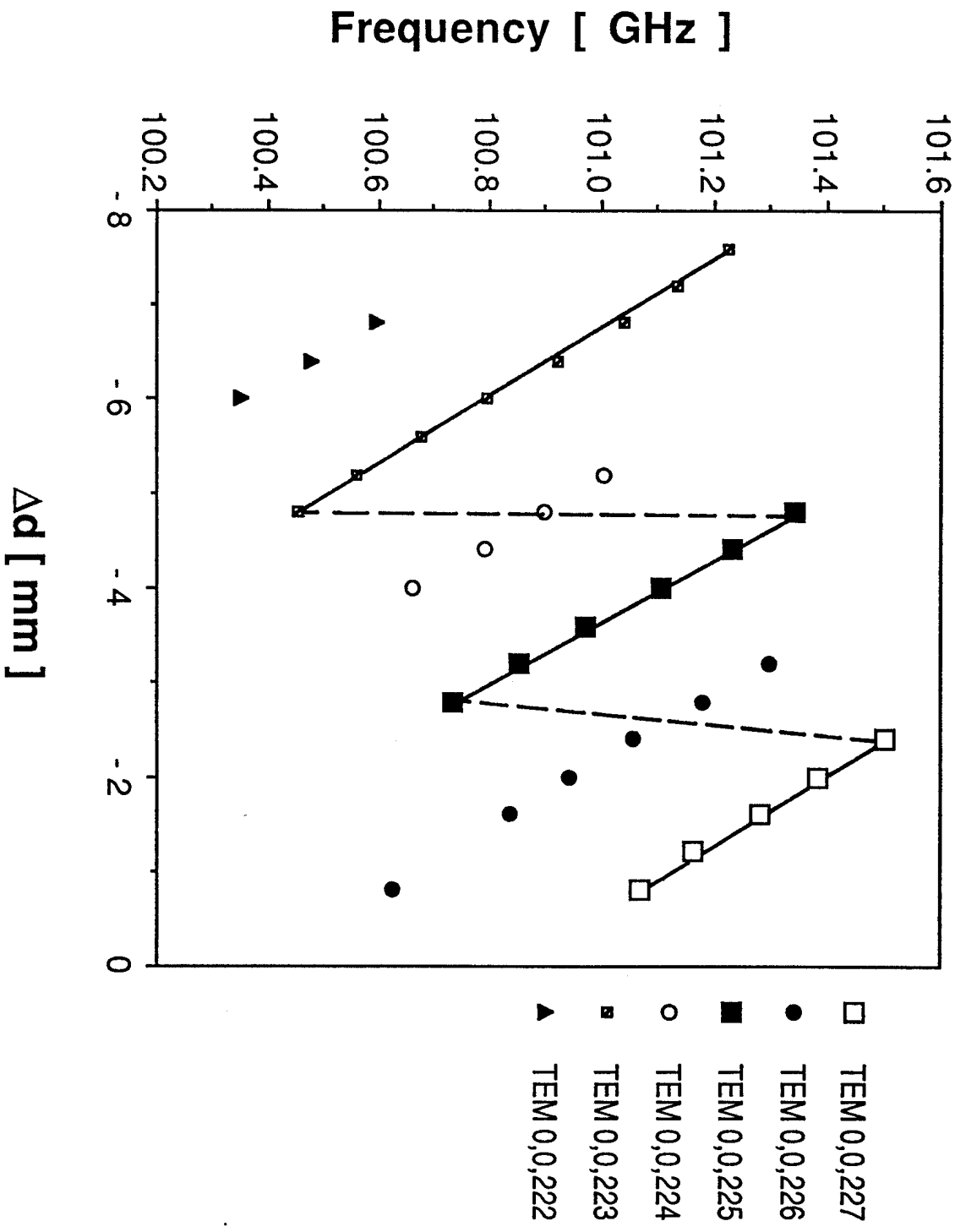
Frequency [GHz]
100.2
100.4
100.6
100.8
101.0
101.2
101.4
101.6
- 8
- 6
- 4
- 2
0
Δd [mm]
TEM 0,0,227
TEM 0,0,226
TEM 0,0,225
TEM 0,0,224
TEM 0,0,223
TEM 0,0,222

FIG. 10

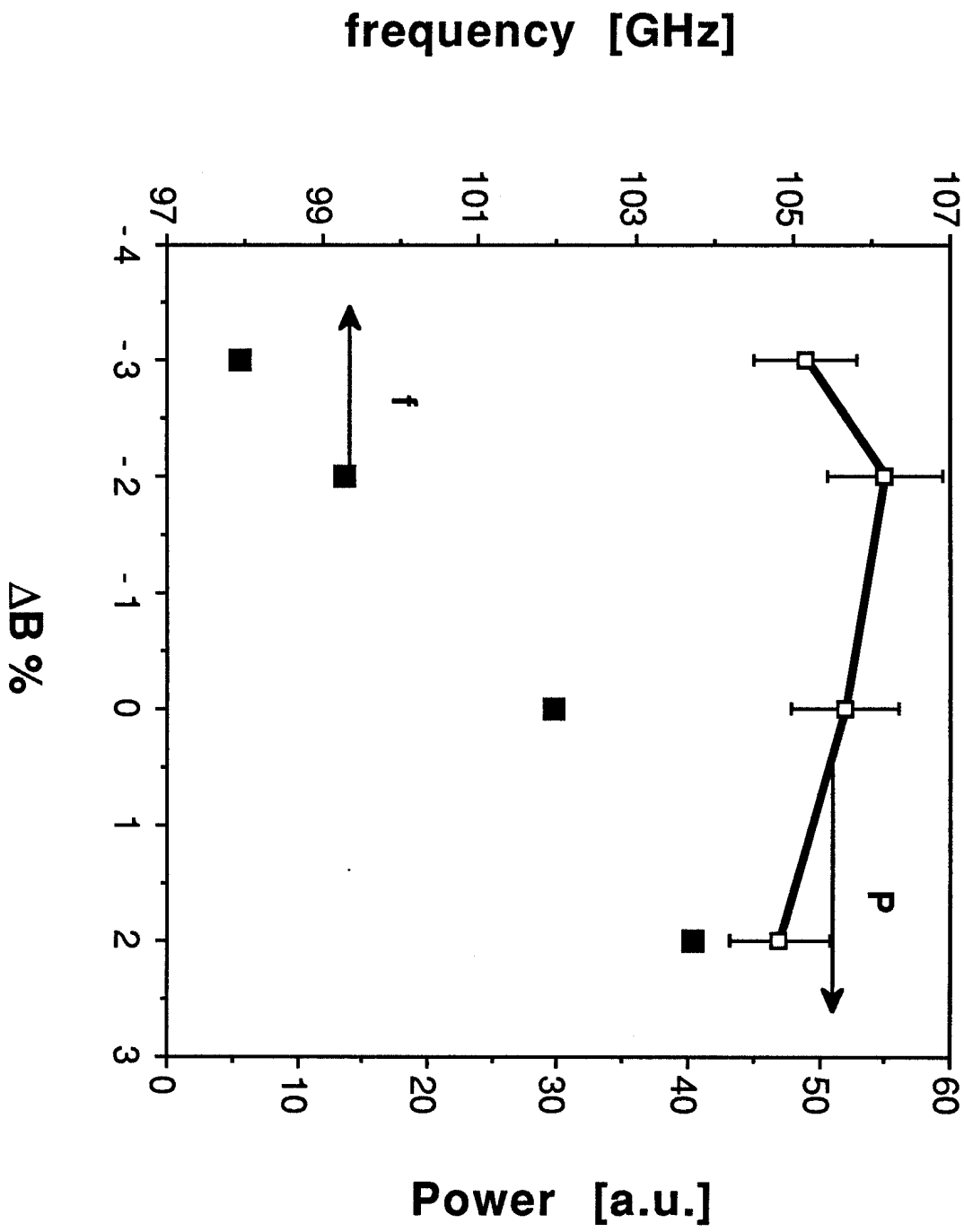
frequency [GHz]
97
99
101
103
105
107
-4
-3
-2
-1
0
1
2
3
ΔB %
f
P
0
10
20
30
40
50
60
Power [a.u.]

FIG. 11

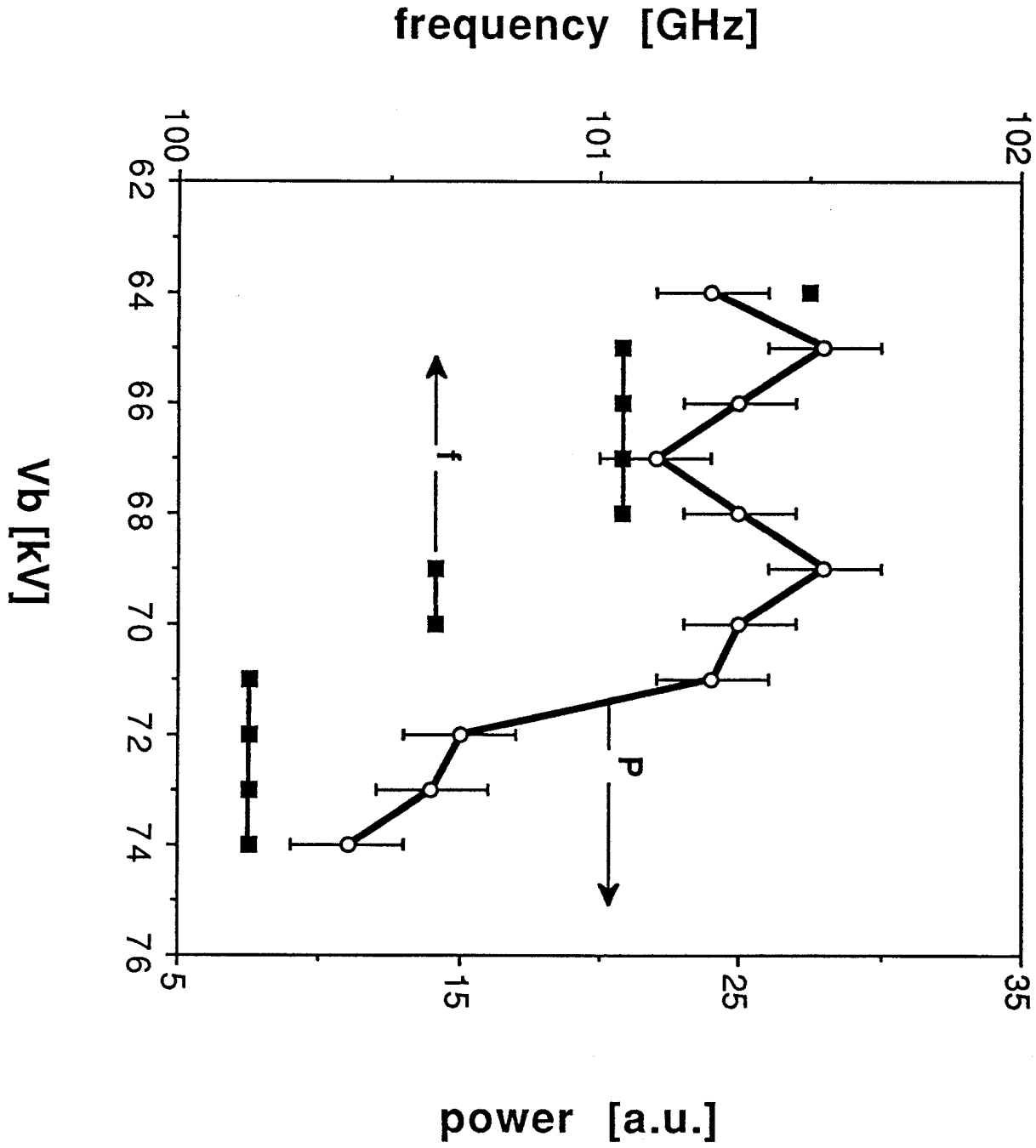
frequency [GHz]
100
101
102
62
64
66
68
70
72
74
76
Vb [kV]
f
P
5
15
25
35
power [a.u.]

FIG. 12

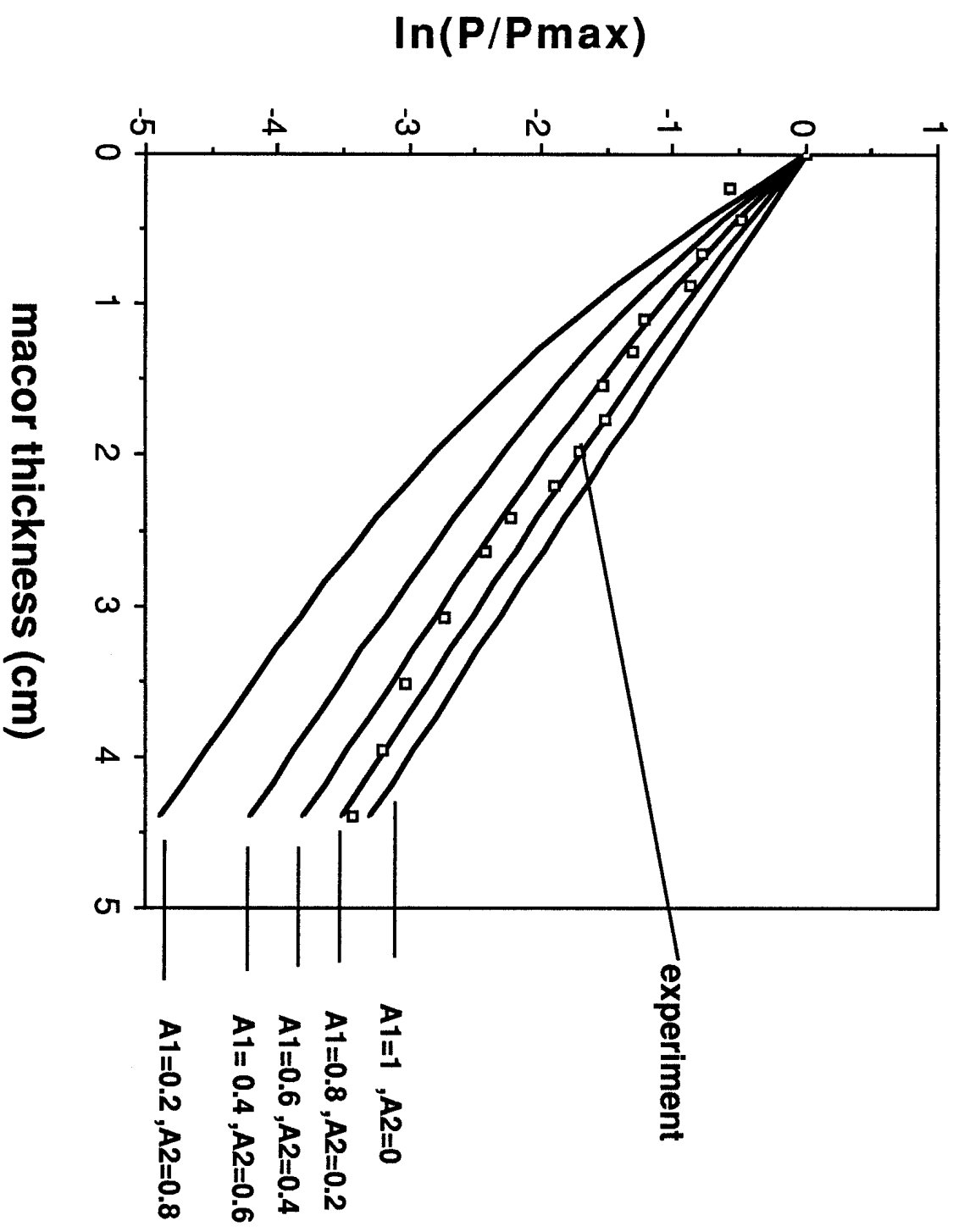
ln(P/Pmax)
1
0
-1
-2
-3
-4
-5
0
1
2
3
4
5
macor thickness (cm)
experiment
A1=1 ,A2=0
A1=0.8 ,A2=0.2
A1=0.6 ,A2=0.4
A1= 0.4 ,A2=0.6
A1=0.2 ,A2=0.8

FIG. 13

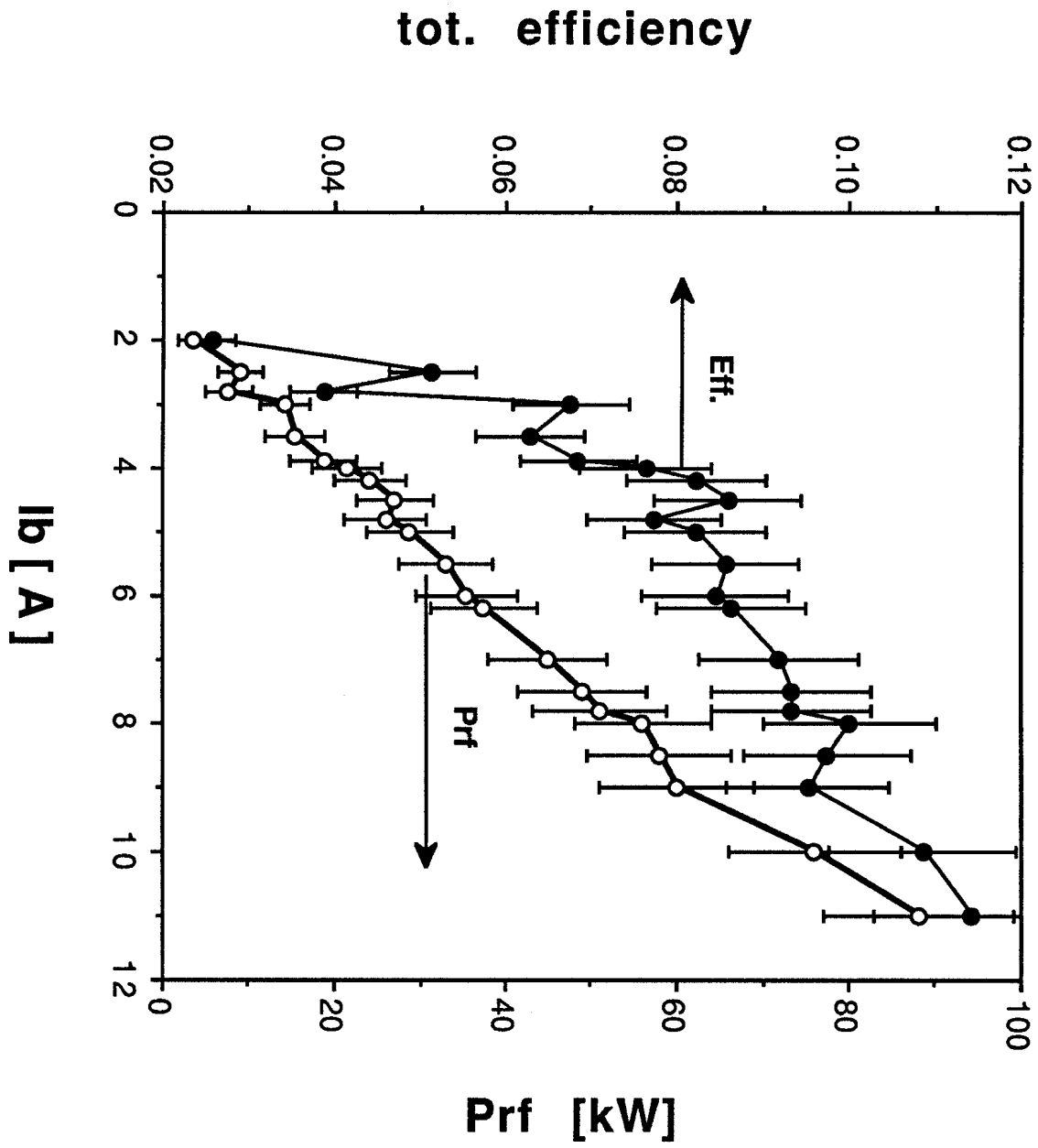
tot. efficiency
0.02
0.04
0.06
0.08
0.10
0.12
Eff.
Prf
Ib [A]
0
2
4
6
8
10
12
0
20
40
60
80
100
Prf [kW]

FIG. 14

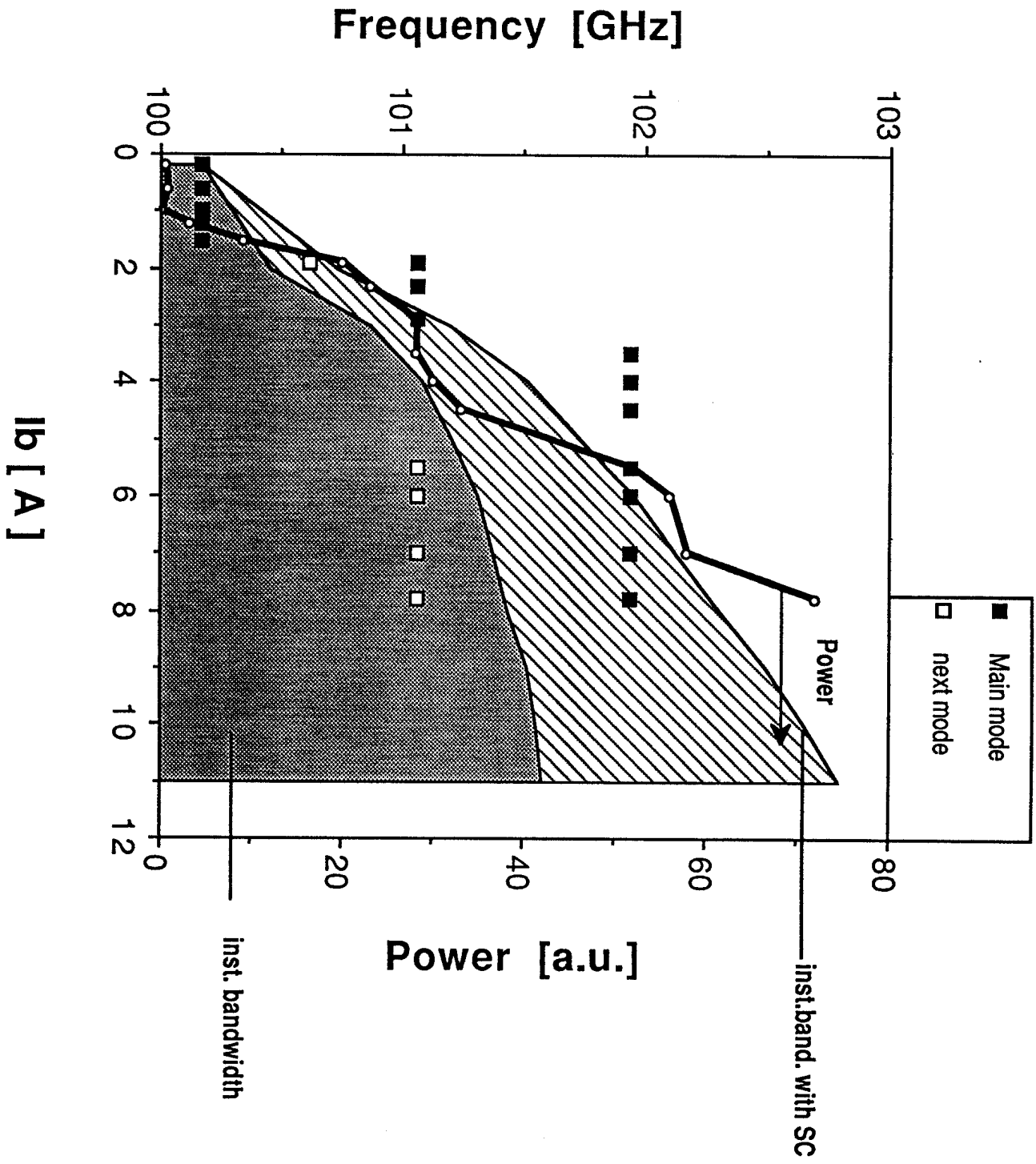
Frequency [GHz]
100
101
102
103
Ib [A]
0
2
4
6
8
10
12
Power [a.u.]
0
20
40
60
80
Main mode
next mode
Power
inst. bandwidth
inst.band. with SC

FIG. 15